

Nano-objects for Addressing the Control of Nanoparticle Arrangement and Performance in Magnetic Hyperthermia

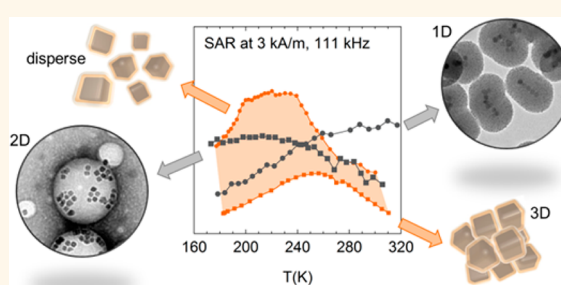
Irene Andreu,[†] Eva Natividad,^{*,†} Laura Solozábal,^{†,§} and Olivier Roubeau[‡]

[†]Instituto de Ciencia de Materiales de Aragón (ICMA), CSIC—Universidad de Zaragoza, Campus Río Ebro, María de Luna 3, 50018 Zaragoza, Spain and

[‡]Instituto de Ciencia de Materiales de Aragón (ICMA), CSIC—Universidad de Zaragoza, Departamento de Física de la Materia Condensada, 50009 Zaragoza, Spain.

[§]Present address for L.S.: Audi AG, Auto-Union-Strasse, 85057 Ingolstadt, Germany.

ABSTRACT One current challenge of magnetic hyperthermia is achieving therapeutic effects with a minimal amount of nanoparticles, for which improved heating abilities are continuously pursued. However, it is demonstrated here that the performance of magnetite nanocubes in a colloidal solution is reduced by 84% when they are densely packed in three-dimensional arrangements similar to those found in cell vesicles after nanoparticle internalization. This result highlights the essential role played by the nanoparticle arrangement in heating performance, uncontrolled in applications. A strategy based on the elaboration of nano-objects able to confine nanocubes in a fixed arrangement is thus considered here to improve the level of control. The obtained specific absorption rate results show that nanoworms and nanospheres with fixed one- and two-dimensional nanocube arrangements, respectively, succeed in reducing the loss of heating power upon agglomeration, suggesting a change in the kind of nano-object to be used in magnetic hyperthermia.



The obtained specific absorption rate results show that nanoworms and nanospheres with fixed one- and two-dimensional nanocube arrangements, respectively, succeed in reducing the loss of heating power upon agglomeration, suggesting a change in the kind of nano-object to be used in magnetic hyperthermia.

KEYWORDS: iron oxide magnetic nanoparticles · PLGA · silica · nano-object · magnetic interactions · specific absorption rate

Magnetic hyperthermia has now become an available anticancer therapy for certain solid tumors, since the recent establishment of the first treatment center at the Charité Hospital in Berlin (NanoTherm therapy).¹ The strictly limited conditions of the approved therapy consist in the injection, directly inside the tumor, of an aqueous solution of aminosilane-coated iron-oxide magnetic nanoparticles (MNPs) of 12 nm diameter, and the application of several hyperthermia sessions using an alternating magnetic field applicator working at 100 kHz in frequency (f) and tunable amplitude (H_0). The goal of these sessions is to generate, during a certain time interval, temperatures high enough to obtain therapeutic effects in the tumor. The achievement of these temperatures depends on the heating ability of the injected MNP properties, on several thermal, physiological, and geometric body parameters, and on H_0 .

Among other challenges, current magnetic hyperthermia must deal with toxicity by achieving adequate maximum temperatures while reducing the MNP dose. One evident approach to achieve this goal would be to increase H_0 during therapies, since more electromagnetic energy would be first absorbed by MNPs and subsequently released as heat. However, the maximum H_0 values that can be safely used are limited by the characteristics of the treated body area, for example, 3–5 kA/m in the pelvic region or 8.5 kA/m in the upper thorax.²

Another approach to limit toxicity and reduce MNP doses consists in using MNPs with high heating abilities at low H_0 values. This approach has represented an active research line during the last years. MNPs with high specific absorption rate (SAR) have been pursued, and high SAR values have been reported in literature like, for example, that of bacterial magnetosomes,³ which show an outstanding SAR of 960 W/g

* Address correspondence to evanat@unizar.es.

Received for review October 10, 2014 and accepted February 6, 2015.

Published online February 06, 2015
10.1021/nn505781f

© 2015 American Chemical Society

at 410 kHz and 10 kA/m or the unprecedented SAR of 415 W/g displayed by synthetic iron/iron carbide core/shell MNPs⁴ at 96 kHz and 16 kA/m, in both cases for colloidal solutions. Also, both are examples of MNPs showing ferromagnetic behavior at room temperature, thus presenting their best heating performance when H_0 exceeds their coercive field, but also the safety limits mentioned above.

It is obvious that the heating ability of an assembly of MNPs is determined by their magnetic properties, since the heat released by MNPs is a consequence of magnetization reversal processes. At the same time, magnetic properties are governed by several MNP characteristics, such as composition, size, shape, and arrangement. For example, the greater saturation magnetization of Fe in the synthetic iron/iron carbide core/shell MNPs with respect to more stable and commonly used iron oxides, together with the synthetic tuning of magnetic anisotropy, is responsible for their excellent heating ability. In magnetosomes, the high SAR values are mainly assigned to the tendency of these MNPs to form long chains, in which their magnetization easy axes are kept parallel with each other, giving rise to a higher magnetic anisotropy.⁵

The effects of composition^{6–8} and size^{9–11} in the heating ability of MNPs have been widely studied, but not that of the shape and even less that of the arrangement. However, the MNP arrangement necessarily plays a very important role in magnetic hyperthermia and, more generally, in theragnosis,¹² since interparticle interactions are known to modify significantly the magnetic behavior expected for MNPs of a given composition, size, and shape. Experimentally, interparticle interactions have been found to be either negative^{12–15} or positive^{5,8,16,17} for the SAR of the assembly. Controlling these effects is certainly of paramount importance in magnetic hyperthermia, since the spatial distribution of MNPs after cell internalization^{18,19} differs from that in ferrofluids, over which SAR measurements are usually performed, thus leading to a divergence between previous characterization and real performance.²⁰ Formation of structures like chains or agglomerates is hardly predictable and reproducible, making it a challenging task to infer heating performance *in vivo*.

In this work, we consider the use of small nano-objects confining a fixed distribution of MNPs, in order to address the control of particle arrangement in magnetic hyperthermia. We first study the effect of the arrangement of free magnetite nanocubes (NCs) in various dispersive media on their magnetic and hyperthermia properties, demonstrating that heating ability is strongly reduced upon agglomeration. We then evaluate the effect of assembling the same NCs within poly(D,L-lactide-co-glycolic) acid (PLGA) nanospheres and silica nanoworms, showing that it is not the concentration but the particular NC arrangements

achieved in these nano-objects that govern their magnetic and hyperthermia properties, making them display an improved behavior with respect to freely arranged agglomerated NCs.

RESULTS AND DISCUSSION

Magnetite Nanocubes. Monodisperse magnetite nanocubes (see below) were prepared through slight modifications of the original seeded growth method of Sun *et al.*²¹ Briefly, initial spherical seeds with a size of 6 nm were obtained by thermal decomposition of iron acetylacetonate in benzyl ether in the presence of oleic acid, oleylamine, and 1,2-hexadecanediol. Then, two identical seeded growth steps were done under similar conditions, but with reduced amounts of oleic acid and oleylamine. The rate of heating, a key parameter with respect to the final nanoparticle's size and shape, was *ca.* 2.5 °C/min. The method is similar to that used by Ern e *et al.* to obtain so-called “facets” nanoparticles,^{22,23} although it results in well-shaped nanocubes in much fewer steps. The direct synthesis of nanocubes has also been described but results in larger sizes, or for smaller sizes requires heating rates as high as 35 °C/min.²⁴

The average size of the obtained nanocubes is 13.2 ± 1.2 nm, as defined by the length of the diagonal of the squares observed in TEM images (see Figure 1), which presumably corresponds to the face diagonal of the cubes. Moreover, the size standard deviation lies within the $\pm 10\%$ criterion for a monodisperse system. It is observed that single cubes coexist with some undefined-shape particles, among them twinned particles, in an approximate proportion of 65:35. Their saturation magnetization, M_s , is 83.2 emu/g (431 kA/m, using a mass density of 5.18 g/cm³), close to the value

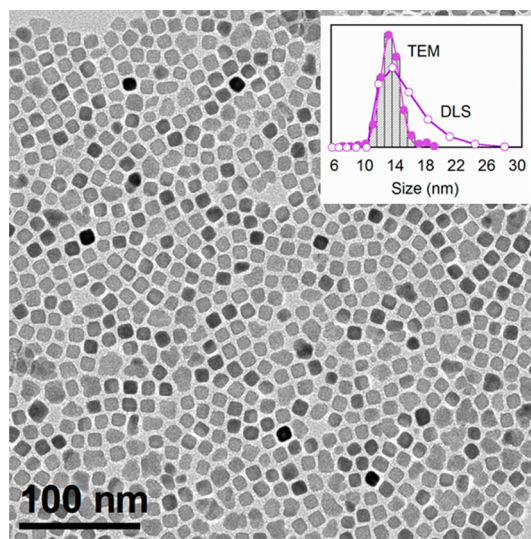
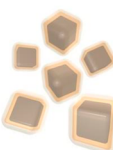

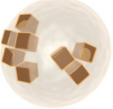
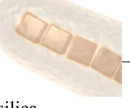


Figure 1. TEM image of a dried drop of hexane dispersion of NCs. Inset: TEM size distribution histogram (bars) fitted to a normal distribution (full circles with line) and DLS hydrodynamic size distribution (empty circles with line) measured on a hexadecane dispersion of the same NCs (sample L-HEXdil, see Table 1).

of bulk magnetite (446 kA/m). Corroboration of the crystalline phase was obtained by powder X-ray diffraction (PXRD) (Figure S1).

Arrangements of Free NCs in Diluted Dispersions. Table 1 gathers forms and concentrations of all samples studied in this work, all made from the same NCs.

TABLE 1. Description of the Studied NC Samples and Their Magnetite Concentration

nano-object	sample ^a	preparation	c (g/g) ^b
	L-HEX	dispersed in n-hexadecane	$5.32 \cdot 10^{-3}$
	L-HEXdil	dispersed in n-hexadecane	$1.78 \cdot 10^{-4}$
	S-TETR	dispersed in n-tetracosane	$5.81 \cdot 10^{-3}$
	S-TETRDil	dispersed in n-tetracosane	$8.40 \cdot 10^{-5}$
NCs as-synthesized	S-SURF	embedded in surfactant	$6.94 \cdot 10^{-1}$
	S-noSURF	embedded in epoxy resin	$9.97 \cdot 10^{-2}$
NCs washed	L-PLGA	dispersed in water	$2.96 \cdot 10^{-4}$
	S-PLGA	freeze-dried powder	$2.96 \cdot 10^{-2}$
PLGA nanospheres	L-SIO2	dispersed in water/ethanol	$4.41 \cdot 10^{-5}$
	S-SIO2	dried powder	$3.25 \cdot 10^{-2}$
silica nanoworms			

^a The first letter of the name reflects the sample state (liquid, L, or solid, S) at room temperature. ^b Concentration is expressed in grams of Fe_3O_4 per gram of sample.

Dispersions were first prepared (see Supporting Information) either in *n*-hexadecane or in *n*-tetracosane. The former undergoes melting over the studied temperature range (10–320 K), while the latter is always solid within this range.

The absence of permanent aggregates at room temperature was corroborated by dynamic light scattering (DLS) over sample L-HEXdil (Figure 1). DLS estimates the hydrodynamic diameter of the nanoparticles, which is usually somewhat larger than the real particle diameter. In the case of L-HEXdil, this diameter shows a log-normal distribution, with sizes lower than the 26 nm of two NC face diagonals, indicating that NCs are well-dispersed, at least in the most dilute *n*-hexadecane solution, since sample L-HEX is too concentrated (Table 1) to be tested with this technique. As a rough estimation, average interparticle distances within L-HEX and L-HEXdil are 91 and 304 nm, respectively, assuming a homogeneous distribution of the NCs.

Samples S-TETR and S-TETRDil were prepared with similar concentrations to L-HEX and L-HEXdil, respectively. TEM images of ultrathin slices of these samples are shown in Figure 2, where the NCs arrangement inside the solid matrixes can be observed. In both samples, isolated NCs but also small arrangements of various dimensionalities are observed, especially in sample S-TETR, indicating that NCs are not ideally dispersed in *n*-tetracosane and that distances between arrangements are larger than evaluated considering isolated NCs.

The magnetic behavior of the samples was studied through zero-field-cooled (ZFC) and field-cooled (FC) magnetization-vs-temperature, $M(T)$, experiments, recorded with a static field of 38 Oe (3 kA/m), equal to the amplitude of the alternating magnetic field used

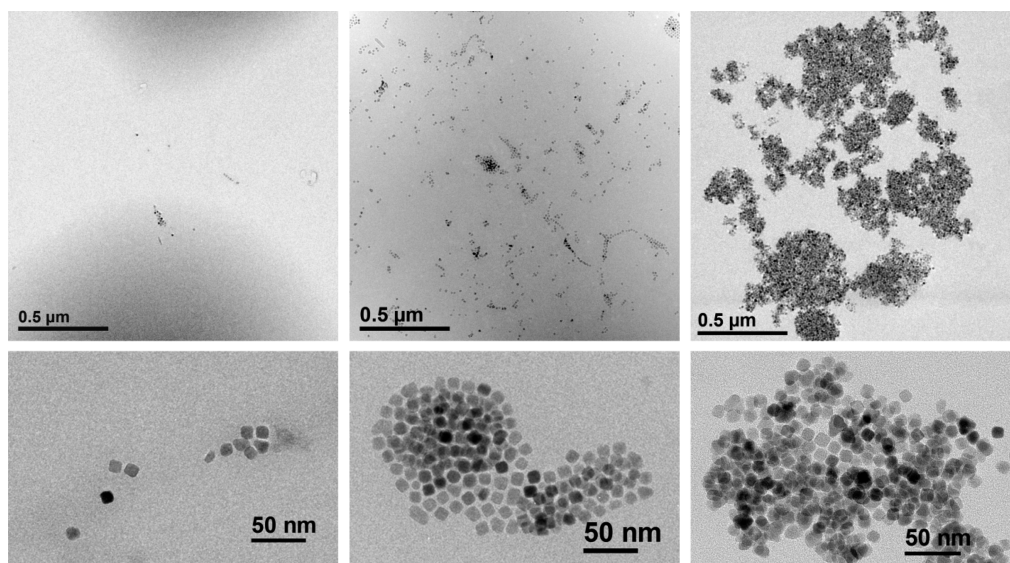


Figure 2. TEM images of ultrathin slices of samples S-TETRDil (left), S-TETR (middle), and S-noSURF (right), revealing the NC arrangements inside solid matrixes.

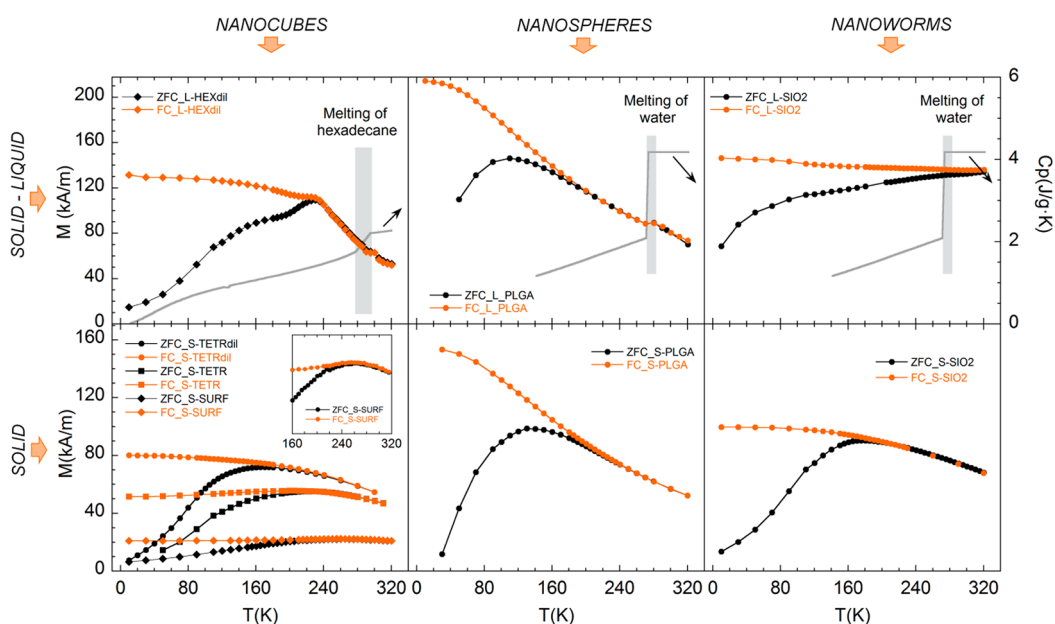


Figure 3. ZFC/FC $M(T)$ curves of the same NCs in several arrangements. Top: Samples with comparable concentration dispersed in media that undergo melting during the studied temperature range. Bottom: Samples either dispersed in solid media or dried from liquid dispersions. Left: Arrangements of isolated NCs. Middle: NCs confined in PLGA nanospheres. Right: NCs confined in silica nanoworms.

TABLE 2. Relevant Temperatures and SAR Values of the Studied Samples

sample	T_{\max} (K) ^a	T_b (K) ^b	SAR_{\max} (W/g) ^c	SAR_{300} (W/g) ^d
L-HEX		250–270	2.9	2.0
L-HEXdil	230			
S-TETR	223	222	2.1	0.9
S-TETRDil	168			
S-SURF	263	253	0.9	0.4
S-noSURF		263	0.7	0.6
L-PLGA	113			
S-PLGA	135	211	1.4	0.8
L-SiO2	>320			
S-SiO2	180	≥315	1.6	1.6

^a Temperature at which ZFC $M(T)$ shows a maximum. ^b Blocking temperature, at which $SAR(T)$ displays a maximum. ^c SAR data at T_b , 3 kA/m, and 111 kHz. ^d SAR data at 300 K, 3 kA/m, and 111 kHz.

in the determination of the heating ability (see below). All measured samples (Figure 3) display a more or less typical behavior of a sample undergoing a ferro(i)-magnetic to superparamagnetic (FM/SPM) transition. On heating, the ZFC $M(T)$ first increases and afterward decreases, showing a maximum at T_{\max} (see Table 2), which corresponds to the average onset of the FM/SPM transition. The ZFC curve joins the FC one at the so-called T_{bra} ,²⁵ the temperature at which all NCs are in the SPM state.

Main differences between samples are related to their T_{\max} values and to the behavior of their FC curve below T_{bra} , which is indicative of magnetic interactions between MNPs.^{25,26} In particular, for noninteracting MNP assemblies, the FC curve is convex below T_{bra} and $M(T)$ shows an appreciable decrease between T_{sat}

(low-temperature value at which M saturates) and T_{bra} . In presence of weak magnetic interactions M at T_{sat} decreases, although the FC curve remains convex. Finally, for strong magnetic interactions, magnetization at T_{sat} is so reduced that the FC curve below T_{bra} describes a plateau or even turns concave, showing a maximum.

According to the behavior of their FC curve, samples S-TETRDil and S-TETR (Figure 3 bottom left) show interaction effects, more pronounced in S-TETR, in which the FC curve appears slightly concave below T_{bra} . Also, the T_{\max} value is greater for S-TETR than for S-TETRDil (Table 2). This shift in T_{\max} is also a consequence of the presence of stronger interactions between NCs. Moreover, the maximum of S-TETR is wider than that of S-TETRDil, indicating a broader distribution of energy barriers for magnetization reversal, in accordance with the wider variety of NC arrangements. Eventually, $M(T)$ values of S-TETR are lower than those of S-TETRDil, another consequence of stronger magnetic interactions.

The ZFC curve of sample L-HEXdil (Figure 3, top left) is similar to that of sample S-TETRDil at low temperature. At about 110 K, its $M(T)$ starts to increase and evolve in a different manner, displaying a double maximum. These features most probably reflect the occurrence of dynamical effects due to a premelting stage of *n*-hexadecane induced by the presence of MNPs.^{27–29} When the slope of the ZFC curve is already decreasing to describe the maximum at T_{\max} , M starts to rise again. At this point, the *n*-hexadecane is likely premolten at the NC surface, allowing the NCs to orientate physically with the applied field, while

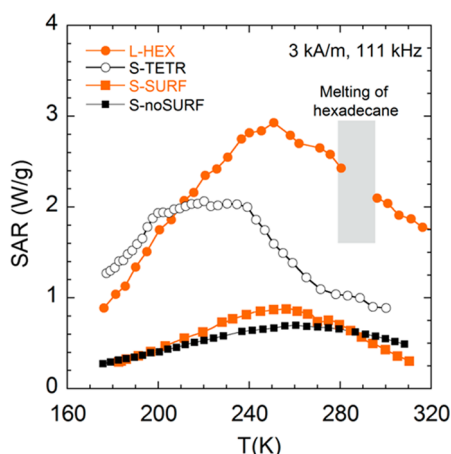


Figure 4. SAR(T) curves of free NCs in different diluted (L-HEX and S-TETR) and concentrated (S-SURF and S-noSURF) arrangements.

preserving a fixed arrangement. As a consequence, the magnetization rises. This effect is even more pronounced in sample L-HEX (Figure S2), giving rise to a higher magnetization increase.

The heating ability of the NC dispersions was evaluated through the calorimetric pulse-heating method under adiabatic conditions, which allows, on one hand, obtaining the most accurate SAR values³⁰ and, on the other hand, obtaining SAR(T) curves,³¹ using the formula

$$\text{SAR}(T) = \frac{C(T) \Delta T(T)}{m_{\text{MNP}} \Delta t} \quad (1)$$

where $\Delta T(T)$ is the thermal dependence of the specimen temperature increments upon application of alternating magnetic field pulses of duration Δt , $C(T)$ is the thermal dependence of the specimen (sample + container) heat capacity, calculated using the mass and specific heat capacity ($\text{J/g} \cdot \text{K}$) of all components of the specimens, and m_{MNP} is the mass of magnetic material, in this case, magnetite. SAR(T) provides information about the FM/SPM transition under alternating magnetic field, similarly to the out-of-phase ac magnetic susceptibility, $\chi''(T)$, curves, but with f and H_0 values more adequate for magnetic hyperthermia (for more details, see the Supporting Information). The too high C/m_{MNP} ratio, however, hindered the determination of the SAR of samples L-HEXdil and S-TETRDil with the used ac-field parameters, 3 kA/m and 111 kHz, selected to fulfill the most widespread biological range of alternating magnetic field application, $fH_0 = 485 \text{ kHz} \cdot \text{kA/m}$.³²

Figure 4 shows, among others, the SAR(T) curves of S-TETR and L-HEX. Data acquired during the melting of *n*-hexadecane were not considered, since the first-order character of the transition prevents a correct evaluation of the heat capacity within the corresponding temperature range. In these curves, the phenomena previously identified in ZFC/FC $M(T)$ are also reflected. Both curves display maxima, corresponding to the

blocking temperature, T_b , defined as the maximum of $\chi''(T)$ and, consequently, of SAR(T), at 111 kHz. S-TETR displays a very broad maximum at an average T_b of 222 K, indicative of the variety of NC arrangements present (Figure 2 middle). The SAR(T) curve of sample L-HEX also shows a broad maximum, with a main maximum at 250 K, and a secondary one at around 270 K, relative to the new arrangement after NC re-orientation due to premelting of *n*-hexadecane.

Regarding absolute values, the NCs dispersed in *n*-hexadecane present the best heating ability due to dynamic effects. The maximum SAR displayed by sample L-HEX is 2.9 W/g. This value may seem very small related to those referred to above, namely, 960 W/g for bacterial magnetosomes or 415 W/g for iron/iron carbide core/shell MNPs, but the power of the alternating magnetic field used here to excite the magnetic moment reversal processes is also much smaller (but adequate for hyperthermia treatment conditions), with an amplitude and frequency of 111 kHz and 3 kA/m, to be compared with 410 kHz and 10 kA/m, and 96 kHz and 16 kA/m, respectively. SAR values depend enormously on f and H_0 , and while this dependence is usually linear with f in the kHz range, it is more complex with H_0 , showing an H_0^n power law, with n ranging between 0 and 3, depending on the characteristics of the MNP assembly and on the value range of H_0 .^{14,33,34} A recent discussion on SAR values and extrapolations²⁹ shows that the SAR of these magnetosomes decreases to 12.8 W/g under the conditions used in this work, while negligible values are reported for iron/iron carbide core/shell MNPs under these conditions, thus making L-HEX a quite good heating dispersion, only about 4 times less than magnetosomes.

Arrangements of Free Highly Packed NCs. Such disperse NC arrangements as those studied so far are however not likely to be achieved in magnetic hyperthermia applications. Indeed, nanoparticles have been shown to adsorb biomolecules on their surface when immersed in biological media,³⁵ thus leading to MNP aggregation and/or cluster formation. Moreover, after being internalized by the cells, MNPs are isolated in vesicles, often in a high concentration. The vesicles are usually on the micrometer size range, confining hundreds of densely packed MNPs, with interparticle distances limited only by their surface molecular coating.^{19,20,36}

Then, in order to study MNP arrangements that are less favorable but more realistic in terms of the therapy conditions, samples S-SURF and S-noSURF have been prepared (Table 1). S-SURF contains the same magnetite NCs just embedded in surfactant (oleic acid and oleylamine). Assuming a homogeneous distribution of the nanocubes inside the surfactant mixture and a surfactant average mass density of 0.854 g/cm^3 , a rough estimation gives an interparticle distance of 5 nm. In S-noSURF, the surfactant not adsorbed onto the nanocubes was eliminated to reduce as much as

possible interparticle distances. Although its average concentration is lower than that of S-SURF due to embedding in epoxy resin, smaller local interparticle distances, of around 1–2 nm, are observed in TEM images (Figure 2, right).

ZFC/FC $M(T)$ curves of S-SURF (Figure 3, bottom left) show an important magnetization decrease with respect to S-TETrdil and S-TETR, as well as an increase in T_{\max} up to 263 K (Table 2). Accordingly, the $SAR(T)$ of this sample (Figure 4) drops drastically with respect to that of samples L-HEX and S-TETR. An even higher SAR drop is observed for sample S-noSURF, together with a T_b increase of 10 K with respect to sample S-SURF. Clearly, the heating capacity of NCs gets strongly reduced upon 3D agglomeration. This implies that, in the event of acquiring an arrangement similar to that of sample S-SURF in tissues, these nanoparticles would lose, at 300 K, 84% of the heating capacity they exhibit in the form of a ferrofluid.

Nano-objects Containing NCs in Fixed 1D and 2D Arrangements. On the basis of the above results, all for the same NCs, it becomes evident that the MNPs' arrangement plays a too important role in their heating performance to be neglected, while it is not controlled in applications. To reach a level of control on the heating ability inside tissues, it thus seems convenient to consider nano-objects able to confine and maintain MNPs (here NCs) in a fixed arrangement.

Among possible confining materials, PLGA and silica were selected. PLGA is a block copolymer known to be biocompatible and noncytotoxic³⁷ and has been previously used for encapsulating MNPs.^{38,39}

Although silica-coated nanoparticles have long been thought to be highly toxic, new studies and synthetic modifications have shown an increased biocompatibility.^{40–42} The growth of silica directly on the NCs' surface has in addition the advantage of freezing the NCs' organization present in the dispersion.⁴³

NCs were thus assembled and confined into two kinds of nano-objects. A first strategy based on a combination of miniemulsion and solvent evaporation techniques⁴⁴ allowed the preparation of polymeric PLGA nano-objects containing NCs, obtained by simply incorporating the dispersed NCs to the organic phase of the emulsion containing the PLGA. In a second approach, the NCs were first transferred to an aqueous-ethanolic dispersion by reaction with tetramethoxyammonium hydroxide.⁴⁵ Addition of tetraethoxysilane and prolonged ultrasonication then resulted in the growth of silica around the NCs,⁴⁶ thus forming nano-objects whose thickness was adjusted so that the average size was comparable to PLGA ones.

The PLGA nano-objects are nanospheres (Figure 5, left) with NCs mostly displaying ordered 2D arrangements located across their surface. This superficial distribution can be inferred from the non-overlapped, clear, and high-contrast NC images observed and also from the presence of several protruding NCs. On the other hand, the silica nano-objects (Figure 5, right) are worm-like, with most NCs in the center and arranged in chains covered with the silica.

PLGA nanospheres, according to TEM images, show a log-normal size distribution with a maximum at 66.1 nm, an average nanosphere size of 67.5 nm, and

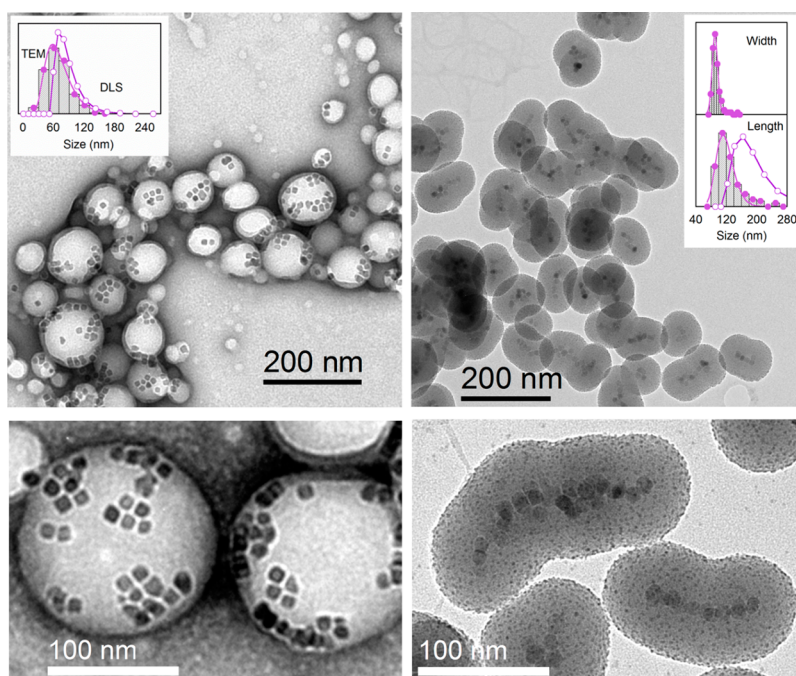


Figure 5. TEM images of PLGA nanospheres (left) and silica nanoworms (right) containing NCs. Insets: TEM size distribution histograms (bars) fitted to normal (nanoworm widths) and log-normal (nanospheres and nanoworm lengths) distributions (full circles with line) and DLS hydrodynamic size distribution (empty circles with line) measured on samples L-PLGA and L-SIO₂.

a standard deviation of 35%. The hydrodynamic diameter follows a similar log-normal distribution with a maximum shifted to 83.8 nm, which indicates that nanospheres are well dispersed in the water solution. Silica nanoworms are elongated, with a well-defined width (normal distribution, with average size of 90.5 ± 7.5 nm) but variable length (log-normal distribution with a maximum at 116 nm and average size of 126 ± 33 nm), depending on the number of NCs involved in the chain. The hydrodynamic diameter also displays a log-normal distribution with a maximum at 175 nm, indicating a good dispersion. Limiting the size of nano-objects was pursued for its importance in applications, since they should remain small enough as to generate minimal microcapillary occlusion in case of transfer to blood circulation.^{47,48} According to the present results, the optimized synthetic conditions have allowed fulfilling this requirement for both types of nano-objects.

Two samples were prepared based on PLGA nanospheres (Table 1), either as a freeze-dried solid, S-PLGA, or as the same freeze-dried solid resuspended in water, L-PLGA. Similarly two samples were obtained from silica nanoworms (Table 1): S-SIO2, made of dried nanoworms, and L-SIO2, which contains nanoworms resuspended in a water–ethanol (18/82 v/v) solution.

Samples L-PLGA and S-PLGA (Figure 3, middle) display a typical FM/SPM transition with just one ZFC maximum. Comparing their T_{\max} data (Table 2) with those of sample S-TETRDil, one concludes that the arrangement of a few NCs into ordered 2D structures has produced a decrease of T_{\max} , this T_{\max} being slightly increased when nanospheres are closer to each other. Unlike all previous cases, the FC curves show an important M decrease from T_{sat} to T_{\max} , indicative of a very weak effect of magnetic interactions. Eventually, the $M(T)$ values of S-PLGA are smaller than those of sample L-PLGA, but remain higher than those of S-SURF and S-TETR. This makes this arrangement particularly interesting, since the change from disperse (liquid) to agglomerated (solid) nanospheres does not imply a huge change in magnetic behavior, minimizing the effect of an inhomogeneous nanosphere spatial distribution in applications.

On the contrary, the ZFC/FC curves of L-SIO2 and S-SIO2 (Figure 3, right) reveal great differences. First, it must be noticed that sample L-SIO2 is not entirely in the superparamagnetic state when it is first cooled to 10 K. This can be inferred from the position of T_{\max} , likely slightly above 320 K, as the ZFC and FC curves are not completely joined at this temperature. This non-superparamagnetic initial state can lead to the presence of some orientation within the sample, which could influence the $M(T)$ values. Nevertheless, it can be clearly concluded that the FC curve of this sample exhibits a plateau below T_{\max} , indicative of strong magnetic interactions, and that the chain structure of the NCs inside each nanoworm shifts the FM/SPM transition to higher temperatures. However,

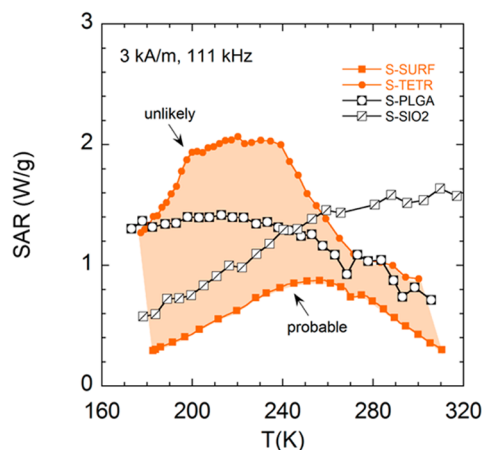


Figure 6. Black symbols: SAR(T) curves of confined NCs in PLGA nanospheres and silica nanoworms in close arrangement. Orange area: SAR variation between slightly (S-TETR) and highly (S-SURF) agglomerated NCs, unlikely and probable situations in magnetic hyperthermia, respectively.

nanoworms in close proximity to each other (sample S-SIO2) present ZFC/FC curves more similar to those of sample S-PLGA, with two main differences: T_{\max} is still higher, and their FC curve still exhibits a plateau below T_{\max} , although less marked than in sample L-SIO2. In other words, interchain interactions seem to modify appreciably the magnetic state of very diluted nanoworms, as opposed to the case of nanospheres. Nonetheless, the $M(T)$ values of S-SIO2 remain higher than those of S-SURF and S-TETR, similarly to those of sample S-PLGA.

As in the case of previous highly diluted samples, the too high C/m_{MNP} ratio hindered the determination of the SAR of samples L-PLGA and L-SIO2 with the used ac-field parameters. In any case, the highly disperse arrangements of these samples are not likely to happen in real magnetic hyperthermia. Figure 6 then collects SAR(T) curves of samples S-PLGA and S-SIO2, in which nanospheres and nanoworms are close together. For comparison, the SAR interval between samples S-TETR and S-SURF has been recalled. This area depicts the SAR variation between slightly (S-TETR) and highly (S-SURF) agglomerated NCs, respectively unlikely and probable situations in magnetic hyperthermia.

The T_b of samples S-PLGA and S-SIO2 is shifted to higher temperatures with respect to T_{\max} values, as expected due to frequency effects. But the most relevant difference between these two samples is the temperature range at which this maximum is achieved, 197–223 K and 309–(\geq)320 K, respectively. From this point of view, the nanoworm configuration of these particular NCs seems more interesting for magnetic hyperthermia than the nanosphere one. However, if NCs big enough to show a FM/SPM transition above room temperature were used, the nanosphere configuration would presumably be more interesting, since it would shift the temperature of the maximum heating ability toward room temperature, while significantly avoiding interaction effects.

Furthermore, comparing the maximum SAR values in the less favorable arrangement, that is, with nano-objects close together, both S-PLGA and S-SIO2 clearly outperform S-SURF, with values of 1.41 and 1.61 W/g, respectively, about 50% of that of sample L-HEX (Figure 4). Eventually, it should be realized that SAR(T) curves of samples S-PLGA and S-SIO2 present very wide maxima. This is due to the also wide distribution of energy barriers, generated by the moderate polydispersity in number and arrangement of the NCs inside each nano-object. A better control of these parameters would result in narrower peaks and greater SAR values.

Considerations about 1D and 2D NCs Arrangements. The results obtained on nanospheres and nanoworms suggest that it is not the concentration but the particular NC arrangements achieved in these nano-objects that govern their magnetic and magnetothermal properties. For example, samples S-PLGA and S-SIO2 have a similar concentration but display opposite behaviors with respect to interactions, as shown by their respective T_{\max} and T_b . Also, both are less and more concentrated than samples S-SURF and S-TETR, respectively, but do not show intermediate M or SAR values.

It has been shown both theoretically⁴⁹ and experimentally⁵⁰ that MNPs self-assembled in chain arrangements tend to display a ferromagnetic order, presenting one or several intrachain FM domains. Given that disperse silica nanoworms (sample L-SIO2) show predominantly a self-assembled NC chain structure, a ferromagnetic order can be assumed. Then, the behavior of sample L-SIO2 can be discussed on the basis of the theoretical calculations proposed in ref 51, which describe the heating efficiency of nanoparticle chains accounting for dipolar interactions in the linear response regime. SAR(σ_0) curves calculated through Monte Carlo simulations for monodisperse particles are quasi-normal distributions whose maximum values get smaller and shift to lower σ_0 as the number of MNPs inside a chain increases, with σ_0 being the reduced energy barrier of the free nanoparticles ($\sigma_0 = E_{b0}/(k_b T)$, where $E_{b0} = K_{\text{eff}}V$ and K_{eff} is the effective anisotropy constant).⁵¹ These findings can be extrapolated to our results as follows. Given that the NC volume is the same in all samples, a decrease in σ_0 upon chain formation must imply either a decrease in K_{eff} or an increase in T . Since the K_{eff} of magnetite decreases when temperature grows,⁵² a shift of SAR(σ_0) to lower σ_0 values implies necessarily a shift of SAR(T) to higher T values, which is consistent with the fact that T_{\max} is higher for sample L-SIO2 than for samples L-HEXdil and S-TETRDil. This shift is indicative of an increase of the energy barrier for magnetization reversal due to the contribution of intrachain dipolar interactions; that is, each NC in the chain has increased its “apparent” anisotropy constant, K_{app} .

The modification of chain properties due to interchain interactions (S-SIO2 vs L-SIO2) has also been

observed in chains of magnetosomes synthesized by magnetotactic bacteria.⁵³ Along this line, magnetic properties at macro- and microscale of arrays of MNP chains have been simulated using a Monte Carlo approach.⁴⁹ Assuming that MNP magnetic anisotropy axes are aligned parallel to the chains and that $H \ll H_A$, where H_A stands for the anisotropy field, simulations predict an intrachain FM order, but a non-monotonic interchain antiferromagnetic order. Although these predictions cannot be strictly extrapolated to sample S-SIO2, in which nanoworms are randomly brought together, the existence of a certain AFM order between chains should not be discarded. Simulations of ZFC/FC curves would be necessary to assign this effect to the reduction in T_{\max} undergone by sample S-SIO2 with respect to L-SIO2.

On the other hand, PLGA nanospheres display several different NC arrangements such as isolated NCs, pairs, and larger 2D arrangements comprising up to approximately 12 NCs. Several experimental and theoretical techniques have been used to study the magnetic configurations of 2D arrangements,^{50,54,55} revealing the occurrence of flux-closure regions in arrangements as small as four similar cubes forming a square, up to islands of 31 spherical MNPs. On the basis of these findings, the existence of flux-closure regions in PLGA nanospheres is a plausible hypothesis. Indeed, in flux-closure configurations of close-packed MNP 2D clusters, magnetic flux is mostly confined within the arrangement,⁵⁶ giving rise to reduced cluster-to-cluster interactions. This is consistent with the low T_{\max} (and, consequently, K_{app}) values of L-PLGA, whose ZFC/FC curves are in addition typical of noninteracting MNPs. Again, simulations of $M(T)$ curves would help to reinforce/discard this hypothesis, which is equally consistent with the weak behavior modification observed when nanospheres are close together (S-PLGA vs L-PLGA).

The present study on NC arrangements still allows one more final consideration, related to the magnetic anisotropy. For example, when comparing cubical with spherical MNPs, some authors^{17,57} find a higher effective anisotropy of cubes with respect to spherical particles, whereas other authors^{7,58} report the contrary. About this discrepancy, it must be mentioned that the theory behind the calculation of the anisotropy constant from magnetic measurements often neglects interparticle interactions, so that the obtained values have to be handled with care. To illustrate this fact, we have estimated the K_{eff} of our NCs in their less interacting arrangements using the Néel and Vogel–Fulcher models (see Supporting Information, Table S1). According to the results obtained for sample L-PLGA ($K_{\text{eff}} = 35.3$ and 21.9 kJ/m³, using Néel and Vogel–Fulcher models, respectively), we can conclude that the NCs studied in this work show a K_{eff} value in the range usually reported for bulk magnetite,

13.5–41 kJ/m³ at room temperature.^{59,60} However, a significant disparity is observed in the results from different samples and models. This leads us to wonder if the obtained discrepancies are originated not only by average concentration⁶⁰ but also by different arrangements even in diluted samples.

CONCLUSIONS

Summarizing, the wide range of magnetic and heating behaviors reported here for the same magnetic NCs demonstrate that not only the concentration but most of all the arrangement of nanoparticles is of paramount importance for hyperthermia, while it is not really controlled in applications. Free NCs dispersed at low concentration in solvents show good heating properties, improved when the dispersive medium undergoes a premelting stage, in which NCs can become oriented with the applied magnetic field while keeping a fixed and disperse arrangement. The formation of big interacting 3D structures at higher concentration implies a shift of the maximum heating power to higher temperatures, but also a drastic reduction in magnetization and heating ability, unfortunately a

situation most likely to also occur *in vivo*. The reported strategy of confining NCs in nano-objects with fixed NC arrangements has succeeded in lessening this performance degradation, also confirming that the particular NC arrangements achieved in these nano-objects govern their magnetic properties and heating ability. In particular, confining NCs as 2D structures on the surface of PLGA nanospheres gives them properties typical of nano-objects displaying weak magnetic interactions, particularly interesting to minimize the effect of an eventual inhomogeneous nanosphere spatial distribution in applications. On the other hand, confining NCs inside silica nanoworms in 1D (chain) structures shifts the maximum heating power to higher temperatures while maintaining high magnetization values. In addition, both kinds of nano-objects outperform the heating ability of free NCs, when considering closely packed arrangements. Eventually, this work highlights the necessity of considering SAR not as a single value at room temperature but as a physical function, whose measurement or simulation as a function of temperature is encouraged, especially for MNPs whose FM/SPM transition is near room temperature.

METHODS

Chemicals. The syntheses were carried out using commercially available reagents. Reagent grade solvents absolute ethanol, chloroform, *n*-hexane (>99%), *n*-hexadecane (99%), and *n*-tetraacosane (99%) were used as received. Benzyl ether (99%), 1,2-hexadecanediol (97%), oleic acid (90%), oleylamine (>70%), Fe(III) acetylacetonate (>99.9% trace metal basis), poly(D,L-lactide-co-glycolide (50:50, MW 30–60k), poly(vinyl alcohol) (MW 13000–23 000), tetraethyl orthosilicate (98%), tetramethylammonium hydroxide pentahydrate (95%), and aqueous ammonia were all purchased from Aldrich and used without further purification.

Synthesis of 6 nm Fe₃O₄ Spherical Nanoparticle Seeds^{21,61}. Fe(acac)₃ (2 mmol), 1,2-hexadecanediol (10 mmol), oleic acid (6 mmol), and oleylamine (6 mmol) were added under a flow of argon to 20 mL of benzyl ether and stirred magnetically at room temperature under Ar for 5 min. The mixture was heated to 200 °C, maintained for 2 h at this temperature, and then heated to reflux (ca. 293 °C) for 1 h, under continuous stirring and flow of Ar. The rate of heating was the maximum attainable with our setup, at ca. 2.5 °C/min. The formed black dispersion was cooled to room temperature by removing the heat source, maintaining stirring. Once at room temperature, the reaction mixture was opened to air, and ethanol (50 mL) was added, resulting in the precipitation of a black solid, which was separated by centrifugation. This raw product was redispersed in hexane (40 mL) in the presence of oleic acid (0.05 mL) and oleylamine (0.05 mL) with bath ultrasonication. After centrifugation to remove undispersed material, the product was then precipitated with ethanol (16 mL), centrifuged to remove the supernatant, and redispersed into hexane (16 mL) with bath ultrasonication. This dispersion was filtered through a 0.45 mm PVDF membrane to remove possible impurities of large size.

Synthesis of 14 nm Fe₃O₄ Nanocubes by Seeded Growth Steps.^{21,23,61} For the first growth step, Fe(acac)₃ (2 mmol), 1,2-hexadecanediol (10 mmol), oleic acid (2 mmol), and oleylamine (2 mmol) were first added under a flow of argon to 20 mL of benzyl ether and stirred magnetically at room temperature under Ar for 5 min. Then 84 mg of the 6 nm seeds dispersed in hexane were added, and the mixture was brought to 100 °C, temperature at which it was kept for 30 min under an argon flow without

condenser to evaporate the hexane. Then, the same thermal steps and workup procedure as for the 6 nm seeds were applied. A second growth step was then realized under identical conditions, except for the amount of the seeds from the previous growth step, which was 80 mg.

Synthesis of PLGA Nanospheres Containing Nanocubes. Polymeric nanospheres loaded with nanocubes were synthesized by a combination of miniemulsion and solvent/evaporation techniques, following a modified procedure from the literature.⁴⁴ 0.5 mL of the original NC dispersion in hexane was evaporated in a vial, yielding 6.17 mg of nanocubes and surfactant. 5 mL of CHCl₃ was added, and the mixture was stirred at 200 rpm for 10 min, resulting in a homogeneous dispersion. Then 50 mg of PLGA was added to the organic suspension and stirred at 400 rpm until no solid polymer was observed. This organic solution was poured onto 10 mL of an aqueous solution of PVA at 5 wt % while stirring at 400 rpm. The formed emulsion was allowed to homogenize by stirring for 1 h at 1000 rpm. The miniemulsion was then prepared by ultrasonication for 10 min with a Hielscher UP400s ultrasonic processor (400 W, 24 kHz) with a 3 mm tip at 35% amplitude. All these steps were performed maintaining the dispersion in an ice bath to prevent chloroform evaporation. Once the miniemulsion was formed, 40 mL of distilled water was added to the dispersion to enhance the evaporation of chloroform by leaving the dispersion at room temperature overnight under magnetic stirring at 750 rpm. The suspension of PLGA nanospheres in water was then filtered. A 10 mL sample of the so-obtained suspension was dialyzed for 24 h with a Float-a-lyzer 300 kDa membrane (SpectrumLabs) to eliminate the excess PVA in the solution. Comparison between the Fe₃O₄ concentration of the nondialyzed (6.03 mg/g) and dialyzed (29.6 mg/g) nanosphere solid indicates that dialysis eliminates about 88% of the total PVA.

Synthesis of Silica Nanoworms Containing Nanocubes. The encapsulation of nanocubes into silica involved two main steps. First, the originally hydrophobic nanoparticles were transferred to water using a recent literature procedure.⁴⁵ Then 6 mg of nanocubes with surfactant was mixed with 5 mL of 1 M TMAOH solution by stirring for 1 h. The obtained suspension was precipitated using a permanent magnet, the supernatant

was removed, and the precipitate was dried in air. For silica encapsulation,⁴⁶ the dry hydrophilic nanocubes were then redispersed in a mixture of 13.5 mL of distilled water and 60 mL of EtOH by 5 min ultrasonic homogenization with a Hielscher UP400s ultrasonic processor (400 W, 24 kHz) with a 3 mm tip at 80% amplitude. After addition of 1.68 mL of aqueous ammonia the solution was allowed another 5 min homogenization. Last, 300 μ L of TEOS was added to the solution, and ultrasonication at 80% was then maintained for 50 min. The thickness of the formed silica shell can be adjusted by modifying the amount of TEOS and/or the sonication time. All the ultrasonication steps were performed while cooling with an ice bath.

Preparation of Samples for Magnetic and SAR Measurements. Samples containing free NCs were prepared from aliquots of the ferrofluid obtained in the synthesis. The *n*-hexane of each aliquot was first evaporated in weighted vials, and the remaining solid was afterward redispersed in the desired dispersive media. Samples L-HEX and L-HEXdil were dispersed in *n*-hexadecane to provide a dispersive medium that, still liquid at room temperature, showed a higher melting temperature than that of *n*-hexane. Once an adequate volume of *n*-hexadecane was added to reach the desired approximate concentration, the vials were ultrasonicated in a water bath for 5 min at room temperature. Samples L-TETR and L-TETRDil were dispersed in *n*-tetracosane to provide a solid dispersive medium in the whole measurement temperature range. The dispersion was performed in a water bath at 100 °C (at which this alkane is already liquid) under ultrasonication with a Hielscher UP200s working at 85% of its maximum power for 30 s using the S3 tip. Sample S-SURF is just the remaining solid after evaporating the *n*-hexane and contains magnetite NCs and surfactant (oleic acid and oleylamine). Sample S-noSURF was obtained in the same way as sample S-SURF, with several additional washing steps with dichloromethane to eliminate as much as possible the surfactant not adsorbed onto the NCs, *i.e.*, to reduce as much as possible interparticle distances. The remaining powder was embedded in epoxy resin (Epofix) and cured at 60 °C for 24 h. The embedding allows a better thermal transfer in SAR measurements, as well as preparation for TEM observation by ultramicrotomy. Sample S-PLGA was obtained from freeze-drying the dialyzed nanosphere solution, and sample L-PLGA was prepared from the same freeze-dried solid resuspended in water. Sample S-SIO2 contains the remaining nanoworms after drying the synthetic solution, and L-SIO2 was obtained by resuspending such nanoworms in a water–ethanol (18/82 v/v) solution. All liquid samples were sealed with adhesive into quartz holders to prevent liquid leakage under vacuum conditions. Sample S-TETR, at 100 °C while filling the quartz holder, was first thermally quenched in an ice–water bath and then sealed with the adhesive. Samples S-SURF, S-PLGA, and S-SIO2 were measured in polypropylene capsules, while sample S-noSURF was measured in its own epoxy resin. The same specimens used for magnetic characterization were used for SAR measurements.

PXRD. Powder X-ray diffraction experiments were performed with a Phillips X'pert Pro diffractometer (Cu K α radiation) on NC powder. Diffraction patterns were recorded in the 2θ range 10–70° with a scan step of 0.05° (2θ) for 5 s.

TEM and DLS. The size and shape of nano-objects were studied by transmission electron microscopy (TEM) with a JEOL 2000 FXII instrument working at an acceleration voltage of 200 kV. Drops of solutions containing NCs, PLGA nanospheres, and silica nanoworms were put onto copper grids with a carbon membrane film. To allow their visibility on TEM, PLGA nanospheres were additionally negatively stained using a 1% solution of phosphotungstic acid in water, whose pH was adjusted to a value between 6.4 and 7.4 by adding small drops of 1 M NaOH. From the acquired images, size histograms were obtained using measurements of at least 300 nano-objects per histogram. The arrangement of NCs dispersed in solid media was also observed by TEM. For this purpose, sample slices were obtained by ultramicrotomy using a diamond knife and laid on similar copper grids. To discard the presence of large permanent aggregates, the hydrodynamic size of nano-objects was determined by DLS on diluted samples using a Zetasizer NanoZS

(Malvern Instruments) in backscatter mode using a 633 nm HeNe laser. From the raw intensity-*vs*-size distributions, number-*vs*-size histograms were obtained using the Rayleigh theory.

Magnetic Characterization. Magnetic characterization was performed using an MPMS-XL superconducting quantum interference device from Quantum Design. Magnetization-*vs*-field, $M(H)$, curves of all samples were measured from 0 to 5 T at 300 K. ZFC/FC $M(T)$ curves were acquired during heating ramps with a static field of 38 Oe (3 kA/m, the same value as H_0 in SAR determination) in the 10–320 K temperature range. The dynamic magnetic properties of several samples were studied through ac susceptibility measurements from 10 to 320 K in the 10–852 Hz frequency range, by applying an alternating magnetic field amplitude of 2.74 Oe. Diamagnetic corrections were applied in all measurements.

Calculation of the Mass of Magnetite. The iron content of some specimens was obtained by inductively coupled plasma-optical emission spectroscopy (ICP-OES, Jobin Yvon 2000). The sample concentration, c (mass of magnetite per mass of sample), was determined combining the results of this elementary analysis with $M(H)$ measurements. After recording its $M(H)$ curve, a sample similar to S-SURF was digested in *aqua regia* at 90 °C and diluted in distilled water up to a volume of 50 mL for ICP-OES analysis. From the obtained Fe value and assuming stoichiometric magnetite composition, the specific saturation magnetization, M_s (emu/g), of the NCs within this sample was determined. The same procedure was applied to another sample similar to S-PLGA. This time two different concentration values were calculated: first, using the Fe content from ICP; second, using the $M(H)$ curve and the specific saturation magnetization obtained from the sample similar to S-SURF. These two values differed by less than 2%, corroborating the validity of the combined ICP- M_s method. The mass of magnetite of the rest of the samples was then calculated dividing their M_s (emu) value by the specific M_s (emu/g) value obtained above.

Heat Capacity Determination for SAR Calculation. The specific heat capacity of the quartz sample holders, adhesive sealant, *n*-tetracosane with dispersed NCs, PLGA nanospheres, silica nanoworms with NCs, and epoxy resin was determined experimentally by differential scanning calorimetry (DSC) using a Q1000 device from TA Instruments and indium and sapphire as calibrants. The specific heat capacities of *n*-hexadecane and magnetite were taken from the literature.^{62–64} The contribution of the oleic acid to the heat capacity has been neglected due to the small mass present in the samples. In sample S-SURF, with the highest oleic acid content, the contribution of the oleic acid to the heat capacity at room temperature gives a difference of only 5% in the SAR value, on the order of the measurement experimental error.

$\Delta T(T)$ Measurements for SAR Calculation. $\Delta T(T)$ measurements in the range 170–320 K were performed with a special-purpose setup⁶⁵ using the pulse-heating method. The samples were first set under vacuum and afterward cooled to 170 K in the absence of an ac field. Then, a gentle heating ramp was established by means of the temperature control of the system, also necessary to ensure that the radiation shield is at the same temperature as the sample, assuring the adiabatic conditions of the experiment. During the heating ramp, ac-field pulses of duration Δt were applied to the samples, which underwent self-heating (ΔT). Ac-field parameters used were $H_0 = 3$ kA/m and $f = 111$ kHz. The calculation procedure of $\Delta T(T)$ is supplied in the Supporting Information.

Conflict of Interest: The authors declare no competing financial interest.

Supporting Information Available: Crystalline phase; dynamic effects of samples L-HEXdil and L-HEX on ZFC/FC $M(T)$; saturation magnetization and hysteresis loop; $\Delta T(T)$ determination procedure for SAR(T) calculation; correlation between SAR and ac susceptibility measurements; estimation of magnetic anisotropy; list of acronyms. This material is available free of charge *via* the Internet at <http://pubs.acs.org>.

Acknowledgment. This work has been funded by the Spanish MINECO and FEDER under projects MAT2007-61621 and MAT2011-24284 and by the University of Zaragoza and

Banco Santander Central Hispano S.A., project UZ2012-CIE-10. I.A. thanks the Spanish CSIC for her JAE-Predoc contract. The use of Servicio General de Apoyo a la Investigación-SAI, Universidad de Zaragoza, is also acknowledged.

REFERENCES AND NOTES

- Maier-Hauff, K.; Ulrich, F.; Nestler, D.; Niehoff, H.; Wust, P.; Thiesen, B.; Orawa, H.; Budach, V.; Jordan, A. Efficacy and Safety of Intratumoral Thermotherapy Using Magnetic Iron-Oxide Nanoparticles Combined with External Beam Radiotherapy on Patients with Recurrent Glioblastoma Multiforme. *J. Neurooncol.* **2011**, *103*, 317–324.
- Thiesen, B.; Jordan, A. Clinical Applications of Magnetic Nanoparticles for Hyperthermia. *Int. J. Hyperther.* **2008**, *24*, 467–474.
- Hergt, R.; Hiergeist, R.; Zeisberger, M.; Schüller, D.; Heyen, U.; Hilger, I.; Kaiser, W. A. Magnetic Properties of Bacterial Magnetosomes as Potential Diagnostic and Therapeutic Tools. *J. Magn. Magn. Mater.* **2005**, *293*, 80–86.
- Meffre, A.; Mehdaoui, B.; Kelsen, V.; Fazzini, P. F.; Carrey, J.; Lachaize, S.; Respaud, M.; Chaudret, B. A Simple Chemical Route toward Monodisperse Iron Carbide Nanoparticles Displaying Tunable Magnetic and Unprecedented Hyperthermia Properties. *Nano Lett.* **2012**, *12*, 4722–4728.
- Alphandéry, E.; Chebbi, I.; Guyot, F.; Durand-Dubief, M. Use of Bacterial Magnetosomes in the Magnetic Hyperthermia Treatment of Tumours: A Review. *Int. J. Hyperther.* **2013**, *29*, 801–809.
- Lee, J.-H.; Jang, J.-t.; Choi, J.-s.; Moon, S. H.; Noh, S.-h.; Kim, J.-w.; Kim, J.-G.; Kim, I.-S.; Park, K. I.; Cheon, J. Exchange-Coupled Magnetic Nanoparticles for Efficient Heat Induction. *Nat. Nanotechnol.* **2011**, *6*, 418–422.
- Noh, S.-h.; Na, W.; Jang, J.-t.; Lee, J.-H.; Lee, E. J.; Moon, S. H.; Lim, Y.; Shin, J.-S.; Cheon, J. Nanoscale Magnetism Control via Surface and Exchange Anisotropy for Optimized Ferrimagnetic Hysteresis. *Nano Lett.* **2012**, *12*, 3716–3721.
- Mehdaoui, B.; Tan, R. P.; Meffre, A.; Carrey, J.; Lachaize, S.; Chaudret, B.; Respaud, M. Increase of Magnetic Hyperthermia Efficiency Due to Dipolar Interactions in Low-Anisotropy Magnetic Nanoparticles: Theoretical and Experimental Results. *Phys. Rev. B* **2013**, *87*, 174419.
- Vázquez-Vázquez, C.; López-Quintela, M. A.; Buján-Núñez, M. C.; Rivas, J. Finite Size and Surface Effects on the Magnetic Properties of Cobalt Ferrite Nanoparticles. *J. Nanopart. Res.* **2011**, *13*, 1663–1676.
- Mehdaoui, B.; Meffre, A.; Carrey, J.; Lachaize, S.; Lacroix, L.-M.; Gougeon, M.; Chaudret, B.; Respaud, M. Optimal Size of Nanoparticles for Magnetic Hyperthermia: A Combined Theoretical and Experimental Study. *Adv. Funct. Mater.* **2011**, *21*, 4573–4581.
- Guardia, P.; Di Corato, R.; Lartigue, L.; Wilhelm, C.; Espinosa, A.; Garcia-Hernandez, M.; Gazeau, F.; Manna, L.; Pellegrino, T. Water-Soluble Iron Oxide Nanocubes with High Values of Specific Absorption Rate for Cancer Cell Hyperthermia Treatment. *ACS Nano* **2012**, *6*, 3080–3091.
- Materia, M. E.; Guardia, P.; Sathya, A.; Pernia Leal, M.; Marotta, R.; Di Corato, R.; Pellegrino, T. Mesoscale Assemblies of Iron Oxide Nanocubes as Heat Mediators and Image Contrast Agents. *Langmuir* **2015**, *31*, 808–816.
- Urtizberea, A.; Natividad, E.; Arizaga, A.; Castro, M.; Mediano, A. Specific Absorption Rates and Magnetic Properties of Ferrofluids with Interaction Effects at Low Concentrations. *J. Phys. Chem. C* **2010**, *114*, 4916–4922.
- Serantes, D.; Baldomir, D.; Martínez-Boubeta, C.; Simeonidis, K.; Angelakeris, M.; Natividad, E.; Castro, M.; Mediano, A.; Chen, D.-X.; Sanchez, A.; Balcells, L.; Martínez, B. Influence of Dipolar Interactions on Hyperthermia Properties of Ferromagnetic Particles. *J. Appl. Phys.* **2010**, *108*, 073918.
- Skumiel, A.; Hornowski, T.; Józefczak, A. Heating Characteristics of Transformer Oil-Based Magnetic Fluids of Different Magnetic Particle Concentrations. *Int. J. Thermophys.* **2011**, *32*, 876–885.
- Hugounenq, P.; Levy, M.; Alloyeau, D.; Lartigue, L.; Dubois, E.; Cabuil, V.; Ricolleau, C.; Roux, S.; Wilhelm, C.; Gazeau, F.; Bazzi, R. Iron Oxide Monocrystalline Nanoflowers for Highly Efficient Magnetic Hyperthermia. *J. Phys. Chem. C* **2012**, *116*, 15702–15712.
- Martinez-Boubeta, C.; Simeonidis, K.; Makridis, A.; Angelakeris, M.; Iglesias, O.; Guardia, P.; Cabot, A.; Yedra, L.; Estrade, S.; Peiro, F.; Saghi, Z.; Midgley, P. A.; Conde-Leboran, I.; Serantes, D.; Baldomir, D. Learning from Nature to Improve the Heat Generation of Iron-Oxide Nanoparticles for Magnetic Hyperthermia Applications. *Sci. Rep.* **2013**, *3*.
- Fortin, J.-P.; Gazeau, F.; Wilhelm, C. Intracellular Heating of Living Cells through Néel Relaxation of Magnetic Nanoparticles. *Eur. Biophys. J.* **2008**, *37*, 223–228.
- Giustini, A. J.; Ivkov, R.; Hoopes, P. J. Magnetic Nanoparticle Biodistribution Following Intratumoral Administration. *Nanotechnology* **2011**, *22*, 345101.
- Di Corato, R.; Espinosa, A.; Lartigue, L.; Tharaud, M.; Chat, S.; Pellegrino, T.; Ménager, C.; Gazeau, F.; Wilhelm, C. Magnetic Hyperthermia Efficiency in the Cellular Environment for Different Nanoparticle Designs. *Biomaterials* **2014**, *35*, 6400–6411.
- Sun, S.; Zeng, H.; Robinson, D. B.; Raoux, S.; Rice, P. M.; Wang, S. X.; Li, G. Monodisperse MFe_2O_4 ($M = Fe, Co, Mn$) Nanoparticles. *J. Am. Chem. Soc.* **2004**, *126*, 273–279.
- Klokkenburg, M.; Vonk, C.; Claesson, E. M.; Meeldijk, J. D.; Erné, B. H.; Philipse, A. P. Direct Imaging of Zero-Field Dipolar Structures in Colloidal Dispersions of Synthetic Magnetite. *J. Am. Chem. Soc.* **2004**, *126*, 16706–16707.
- Luigjes, B.; Woudenberg, S. M. C.; de Groot, R.; Meeldijk, J. D.; Torres Galvis, H. M.; de Jong, K. P.; Philipse, A. P.; Erné, B. H. Diverging Geometric and Magnetic Size Distributions of Iron Oxide Nanocrystals. *J. Phys. Chem. C* **2011**, *115*, 14598–14605.
- Yang, H.; Ogawa, T.; Hasegawa, D.; Takahashi, M. Synthesis and Magnetic Properties of Monodisperse Magnetite Nanocubes. *J. Appl. Phys.* **2008**, *103*, 07D526.
- Dormann, J. L.; Fiorani, D.; Tronc, E. Magnetic Relaxation in Fine-Particle Systems. In *Advances in Chemical Physics*; Progogine, I.; Rice, S. A., Eds.; John Wiley & Sons: Hoboken, NJ, USA, 2007; Vol. 98, pp 283–494.
- Papuso, C., Jr. The Particle Interaction Effects in the Field-Cooled and Zero-Field-Cooled Magnetization Processes. *J. Magn. Magn. Mater.* **1999**, *195*, 708–732.
- Cheng, G.; Dennis, C. L.; Shull, R. D.; Walker, A. R. H. Influence of the Colloidal Environment on the Magnetic Behavior of Cobalt Nanoparticles. *Langmuir* **2007**, *23*, 11740–11746.
- Wen, T.; Liang, W.; Krishnan, K. M. Coupling of Blocking and Melting in Cobalt Ferrofluids. *J. Appl. Phys.* **2010**, *107*, 09B501.
- Andreu, I.; Natividad, E.; Ravagli, C.; Castro, M.; Baldi, G. Heating Ability of Cobalt Ferrite Nanoparticles Showing Dynamic and Interaction Effects. *RSC Adv.* **2014**, *4*, 28968–28977.
- Andreu, I.; Natividad, E. Accuracy of Available Methods for Quantifying the Heat Power Generation of Nanoparticles for Magnetic Hyperthermia. *Int. J. Hyperther.* **2013**, *29*, 739–751.
- Natividad, E.; Castro, M.; Mediano, A. Adiabatic Magnetothermia Makes Possible the Study of the Temperature Dependence of the Heat Dissipated by Magnetic Nanoparticles under Alternating Magnetic Fields. *Appl. Phys. Lett.* **2011**, *98*, 243119.
- Atkinson, W. J.; Brezovich, I. A.; Chakraborty, D. P. Usable Frequencies in Hyperthermia with Thermal Seeds. *IEEE Trans. Biomed. Eng.* **1984**, *BME-31*, 70–75.
- Carrey, J.; Mehdaoui, B.; Respaud, M. Simple Models for Dynamic Hysteresis Loop Calculations of Magnetic Single-Domain Nanoparticles: Application to Magnetic Hyperthermia Optimization. *J. Appl. Phys.* **2011**, *109*, 083921.
- Müller, R.; Dutz, S.; Neeb, A.; Cato, A. C. B.; Zeisberger, M. Magnetic Heating Effect of Nanoparticles with Different

- Sizes and Size Distributions. *J. Magn. Magn. Mater.* **2013**, *328*, 80–85.
35. Tenzer, S.; Docter, D.; Kuharev, J.; Musyanovych, A.; Fetz, V.; Hecht, R.; Schlenk, F.; Fischer, D.; Kiouptsi, K.; Reinhardt, C.; Landfester, K.; Schild, H.; Maskos, M.; Knauer, S. K.; Stauber, R. H. Rapid Formation of Plasma Protein Corona Critically Affects Nanoparticle Pathophysiology. *Nat. Nanotechnol.* **2013**, *8*, 772–781.
 36. Sanchez, C.; El Hajj Diab, D.; Connord, V.; Clerc, P.; Meunier, E.; Pipy, B.; Payré, B.; Tan, R. P.; Gougeon, M.; Carrey, J.; Gigoux, V.; Fourmy, D. Targeting a G-Protein-Coupled Receptor Overexpressed in Endocrine Tumors by Magnetic Nanoparticles to Induce Cell Death. *ACS Nano* **2014**, *8*, 1350–1363.
 37. Anderson, J. M.; Shive, M. S. Biodegradation and Biocompatibility of PLA and PLGA Microspheres. *Adv. Drug Delivery Rev.* **1997**, *28*, 5–24.
 38. Okassa, L. N.; Marchais, H.; Douziech-Eyrolles, L.; Hervé, K.; Cohen-Jonathan, S.; Munnier, E.; Soucé, M.; Linassier, C.; Dubois, P.; Chourpa, I. Optimization of Iron Oxide Nanoparticles Encapsulation within Poly(D,L-Lactide-Co-Glycolide) Sub-Micron Particles. *Eur. J. Pharm. Biopharm.* **2007**, *67*, 31–38.
 39. Patel, D.; Moon, J. Y.; Chang, Y.; Kim, T. J.; Lee, G. H. Poly(D,L-Lactide-Co-Glycolide) Coated Superparamagnetic Iron Oxide Nanoparticles: Synthesis, Characterization and *in Vivo* Study as MRI Contrast Agent. *Colloids Surf., A* **2008**, *313–314*, 91–94.
 40. Herd, H. L.; Malugin, A.; Ghandehari, H. Silica Nanoconstruct Cellular Tolerant Threshold. *In Vitro J. Contr. Release* **2011**, *153*, 40–48.
 41. Singh, R. K.; Kim, T.-H.; Patel, K. D.; Knowles, J. C.; Kim, H.-W. Biocompatible Magnetite Nanoparticles with Varying Silica-Coating Layer for Use in Biomedicine: Physicochemical and Magnetic Properties, and Cellular Compatibility. *J. Biomed. Mater. Res., A* **2012**, *100A*, 1734–1742.
 42. Otero-Lorenzo, R.; Davila-Ibanez, A. B.; Comesana-Hermo, M.; Correa-Duarte, M. A.; Salgueirino, V. Synergy Effects of Magnetic Silica Nanostructures for Drug Delivery Applications. *J. Mater. Chem. B* **2014**, *2*, 2645–2653.
 43. Mahtab, F.; Yu, Y.; Lam, J. W. Y.; Liu, J.; Zhang, B.; Lu, P.; Zhang, X.; Tang, B. Z. Fabrication of Silica Nanoparticles with Both Efficient Fluorescence and Strong Magnetization and Exploration of Their Biological Applications. *Adv. Funct. Mater.* **2011**, *21*, 1733–1740.
 44. Urban, M.; Musyanovych, A.; Landfester, K. Fluorescent Superparamagnetic Polylactide Nanoparticles by Combination of Miniemulsion and Emulsion/Solvent Evaporation Techniques. *Macromol. Chem. Phys.* **2009**, *210*, 961–970.
 45. Park, J. C.; Gilbert, D. A.; Liu, K.; Louie, A. Y. Microwave Enhanced Silica Encapsulation of Magnetic Nanoparticles. *J. Mater. Chem.* **2012**, *22*, 8449–8454.
 46. Zhang, F.; Wang, C.-C. Fabrication of One-Dimensional Iron Oxide/Silica Nanostructures with High Magnetic Sensitivity by Dipole-Directed Self-Assembly. *J. Phys. Chem. C* **2008**, *112*, 15151–15156.
 47. Hallmark, B.; Darton, N. J.; Han, X.; Palit, S.; Mackley, M. R.; Slater, N. K. H. Observation and Modelling of Capillary Flow Occlusion Resulting from the Capture of Superparamagnetic Nanoparticles in a Magnetic Field. *Chem. Eng. Sci.* **2008**, *63*, 3960–3965.
 48. Elsbahy, M.; Wooley, K. L. Design of Polymeric Nanoparticles for Biomedical Delivery Applications. *Chem. Soc. Rev.* **2012**, *41*, 2545–2561.
 49. Serantes, D.; Baldomir, D.; Pereiro, M.; Hernando, B.; Prida, V. M.; Llamazares, J. L. S.; Zhukov, A.; Ilyn, M.; González, J. Magnetic Ordering in Arrays of One-Dimensional Nanoparticle Chains. *J. Phys. D: Appl. Phys.* **2009**, *42*, 215003.
 50. Varón, M.; Beleggia, M.; Kasama, T.; Harrison, R. J.; Dunin-Borkowski, R. E.; Puentes, V. F.; Frandsen, C. Dipolar Magnetism in Ordered and Disordered Low-Dimensional Nanoparticle Assemblies. *Sci. Rep.* **2013**, *3*, 1234.
 51. Branquinho, L. C.; Carrião, M. S.; Costa, A. S.; Zufelato, N.; Sousa, M. H.; Miotto, R.; Ivkov, R.; Bakuzis, A. F. Effect of Magnetic Dipolar Interactions on Nanoparticle Heating Efficiency: Implications for Cancer Hyperthermia. *Sci. Rep.* **2013**, *3*, 2887.
 52. Cullity, B. D.; Graham, C. D. *Introduction to Magnetic Materials*, 2nd ed.; Wiley: Hoboken, NJ, USA, 2009.
 53. Alphanbéry, E.; Ngo, A. T.; Lefèvre, C.; Lisiecki, I.; Wu, L. F.; Pileni, M. P. Difference between the Magnetic Properties of the Magnetotactic Bacteria and Those of the Extracted Magnetosomes: Influence of the Distance between the Chains of Magnetosomes. *J. Phys. Chem. C* **2008**, *112*, 12304–12309.
 54. Georgescu, M.; Klokkenburg, M.; Erné, B. H.; Liljeroth, P.; Vanmaekelbergh, D.; Zeijlmans van Emmichoven, P. A. Flux Closure in Two-Dimensional Magnetite Nanoparticle Assemblies. *Phys. Rev. B* **2006**, *73*, 184415.
 55. Snoeck, E.; Gatel, C.; Lacroix, L. M.; Blon, T.; Lachaize, S.; Carrey, J.; Respaud, M.; Chaudret, B. Magnetic Configurations of 30 nm Iron Nanocubes Studied by Electron Holography. *Nano Lett.* **2008**, *8*, 4293–4298.
 56. Wei, A.; Kasama, T.; Dunin-Borkowski, R. E. Self-Assembly and Flux Closure Studies of Magnetic Nanoparticle Rings. *J. Mater. Chem.* **2011**, *21*, 16686–16693.
 57. Chou, S.-W.; Zhu, C.-L.; Neeleshwar, S.; Chen, C.-L.; Chen, Y.-Y.; Chen, C.-C. Controlled Growth and Magnetic Property of FePt Nanostructure: Cuboctahedron, Octapod, Truncated Cube, and Cube. *Chem. Mater.* **2009**, *21*, 4955–4961.
 58. Salazar-Alvarez, G.; Qin, J.; Šepelák, V.; Bergmann, I.; Vasilakaki, M.; Trohidou, K. N.; Ardisson, J. D.; Macedo, W. A. A.; Mikhaylova, M.; Muhammed, M.; Baró, M. D.; Nogués, J. Cubic versus Spherical Magnetic Nanoparticles: The Role of Surface Anisotropy. *J. Am. Chem. Soc.* **2008**, *130*, 13234–13239.
 59. Rosensweig, R. E. Heating Magnetic Fluid with Alternating Magnetic Field. *J. Magn. Magn. Mater.* **2002**, *252*, 370–374.
 60. Calero-Diaz del Castillo, V. L.; Rinaldi, C. Effect of Sample Concentration on the Determination of the Anisotropy Constant of Magnetic Nanoparticles. *IEEE Trans. Magn.* **2010**, *46*, 852–859.
 61. Sun, S.; Zeng, H. Size-Controlled Synthesis of Magnetite Nanoparticles. *J. Am. Chem. Soc.* **2002**, *124*, 8204–8205.
 62. Douslin, D. R.; Huffman, H. M. Low-Temperature Thermal Data on the Five Isomeric Hexanes. *J. Am. Chem. Soc.* **1946**, *68*, 1704–1708.
 63. Finke, H. L.; Gross, M. E.; Waddington, G.; Huffman, H. M. Low-Temperature Thermal Data for the Nine Normal Paraffin Hydrocarbons from Octane to Hexadecane. *J. Am. Chem. Soc.* **1954**, *76*, 333–341.
 64. Westrum, E. F., Jr.; Grønvold, F. Magnetite (Fe₃O₄) Heat Capacity and Thermodynamic Properties from 5 to 350 K, Low-Temperature Transition. *J. Chem. Thermodyn.* **1969**, *1*, 543–557.
 65. Natividad, E.; Castro, M.; Mediano, A. Accurate Measurement of the Specific Absorption Rate Using a Suitable Adiabatic Magnetothermal Setup. *Appl. Phys. Lett.* **2008**, *92*, 093116.